

Article

# Research on the Flexural Behavior of a Coastwise RS-OCT Beam That Has Endured Long-Term Fatigue Load for Years

Dongxu Hou <sup>1</sup>, Tieming Hu <sup>1,\*</sup>, Guanhua Zhang <sup>2</sup>, Feng Jiang <sup>3</sup> and Liujie Wang <sup>1</sup>

<sup>1</sup> Construction Engineering Department, Shenyang University, Shenyang 110044, China

<sup>2</sup> Liaoning Provincial Transportation Planning and Design Institute Co., Ltd., Shenyang 110057, China

<sup>3</sup> Shenyang Construction Quality Testing Centre Co., Ltd., Shenyang 110004, China

\* Correspondence: hu\_tm@163.com

**Abstract:** Retrofitted super-span old T-shaped concrete beams (RS-OCT beams) are commonly used in highway bridges in coastal cities and offshore zones in China. The realization of a practical ultimate state for this beam under a bending load is still lacking. In this study, a flexural experiment on an original RS-OCT beam subjected to a long-term vehicle cyclical load was conducted in a laboratory. Several interesting phenomena were discovered. Notably, a butt-weld joint typically exists on longitudinal reinforced bars, which may be vulnerable to bending. The RS-OCT beam simultaneously suffered from the double function of atmospheric environment and fatigue during service. Based on the time-dependent and fatigue theories of materials, finite element analysis was performed using the ABAQUS software. The flexural behavior of the RS-OCT beam at various time periods was simulated. Subsequently, the flexural bearing capacities of the beams were calculated. The safety reservation of the RS-OCT beam at various time stages was related to the change in material properties and upgrading of the loading level. The latter plays a dominant role in the service state.

**Keywords:** RS-OCT beam; coastal region; flexural behavior; long-term; fatigue



**Citation:** Hou, D.; Hu, T.; Zhang, G.; Jiang, F.; Wang, L. Research on the Flexural Behavior of a Coastwise RS-OCT Beam That Has Endured Long-Term Fatigue Load for Years. *J. Mar. Sci. Eng.* **2023**, *11*, 1511. <https://doi.org/10.3390/jmse11081511>

Academic Editor: Francesco Fabbrocino

Received: 10 June 2023

Revised: 10 July 2023

Accepted: 24 July 2023

Published: 29 July 2023



**Copyright:** © 2023 by the authors. Licensee MDPI, Basel, Switzerland. This article is an open access article distributed under the terms and conditions of the Creative Commons Attribution (CC BY) license (<https://creativecommons.org/licenses/by/4.0/>).

## 1. Introduction

Super-span (20 or 30 m) reinforced concrete T-beams have been widely adopted in old Chinese highway bridges in coastal cities and offshore regions. T-beams, without a pre-stressed technique, with a special layout of reinforcement bars, were commonly built in the 1980s–1990s. Currently, most beams still bear cyclical vehicle loads by means of regular maintenance and necessary reinforcement. The mechanical performance of the RS-OCT beams is important for the safety and reliability of bridge structures.

Many performances of retrofitted reinforced concrete (RC) T-beams have been reported by related research [1–12]. FRP materials have a positive effect on the capacity of the RC T-beam [1–3], whether they are normal concrete or lightweight concrete specimens. The percentage increase in flexural capacity is more evident in normal-weight beams as the number of layers increases [4]. However, for RC T-beams in flexure, the retrofitting effect depends on the coordination between the specimen and FRP. FRP debonding is a type of failure involving large deformations of T-beams during bending [5]. Related research has shown that attaching CFRP sheets and assisting with CFRP splay anchors are effective in improving the flexural capacity of T-beams [6], and that the assisting external double-steel channel can also improve the flexural capacity of the T-beam [7]. NSM is another method for improving flexural bearing capacity [8,9]. T-beams have special characteristics in which the flange plays an important role in the flexural bearing capacity. Many recent studies have focused on the taste of flanges using new materials [10,11]. It was verified that the FRP and NSM methods are effective in improving the flexural performance of RC T-beams.

A T-beam is an important part of a highway bridge and is subjected to cyclical vehicle loads for a long time. The fatigue performance of retrofitted RC beams has been extensively

studied [12–14]. The fatigue performance of RC beams is related to the fatigue performance of the concrete and steel bars. Generally, the fatigue damage that occurred in the concrete or steel bars caused fatigue damage in the RC specimen. Therefore, studies on the fatigue performance of concrete and reinforced bars were the basis for these specimens. Related studies have shown that the fatigue performance of concrete depends on aging, curing conditions, stress amplitude, concrete strength, loading frequency, and other factors. The fatigue strength of concrete increases when the fatigue load is lower than the ultimate fatigue load [15]. The fatigue life of concrete decreases as the compressive strength increases [16]. The fatigue life of the concrete at high frequencies was greater than that at low frequencies [17]. The fatigue performance of the reinforced bars is more important. Under a fatigue load, an RC beam is broken by the brittle fracture of tensile steel bars [18]. It is generally believed that the stress amplitude of a reinforcement directly affects its fatigue life.

As previously mentioned, most studies have focused on the retrofitting effects of RC T-beams. The fatigue behavior of RC T-beams has also been reported by many researchers. However, few studies have focused on the flexural behavior of FRP-retrofitted RC T-beams subjected to cyclic loads for many years. Additionally, many existing theories and conclusions have been sourced from experimental studies in which ideal, casting-in-laboratory, and reduced-scale models are used. However, the actual ultimate state and failure procedures of RS-OCT beams have not been clearly recognized. To fill this gap, this study focuses on the flexural behavior of RS-OCT beams over their entire service life, considering the influence of the atmospheric environment and fatigue function. A flexural behavior experiment using an original RS-OCT beam cut down from a bridge was carried out in the laboratory. Finite element analysis using the ABAQUS software resulted in many new and worthy conclusions regarding the flexural behavior of RS-OCT beams.

## 2. Experiment on an RS-OCT Beam

### 2.1. Specimen Preparation

RS-OCT beams are commonly used in highway bridges in Chinese coastal cities and offshore regions. The specimen used in the study was obtained from a 33-year-old bridge from a coastal region. The bridge, with a length of 1500 m, was built in 1991 and reinforced in 2005, as seen in Figure 1. A simply supported T-beam was used as the main girder of the superstructure. In this study, a T-beam was taken from the original bridge as a specimen.



**Figure 1.** Super-span original bridge.

The original RS-OCT beam with a super span of 20 m is a precast specimen. According to an engineering document, the body and upper pavement of the original beam were made of 250# concrete (nearly 23 MPa) with a special layout of inner reinforced bars. In 2005, the T-beam was retrofitted by recasting the pavement with C40 concrete and attaching 1-layer GFRP strips to the bottom of the T-beam, combined with five oblique U-strips on both sides. The actual dimensions and material properties of the specimen were determined through engineering testing. The details of these parameters are presented in Figure 2 and Table 1. The data in Figure 2 are all measured in mm, and measurements were made at least three times.

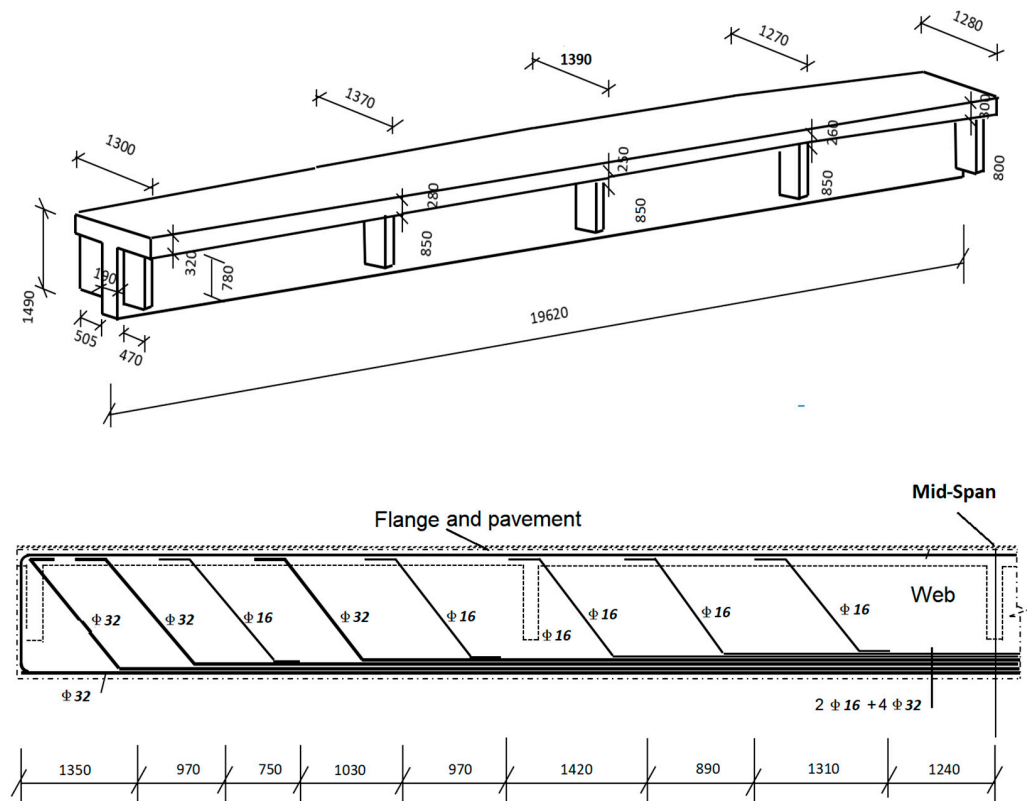


Figure 2. Actual dimension of the specimen and inner reinforced bars.

Table 1. Main parameters of the materials.

	$f_{cb}/$ MPa	$f_{cp}/$ MPa	$f_y/$ MPa	$f_u/$ MPa	$E_s/$ GPa	$f_{GFRP}/$ MPa	$E_{GFRP}/$ GPa
Initial value	22.4	42.0	360.0 (nominal)	585.0 (nominal)	210.0 (nominal)	–	–
Measured value current period	31.2	45.9	320.7	521.3	215.2	800 (nominal)	80 (nominal)

In Table 1,  $f_{cb}$  and  $f_{cp}$  represent the compressive strengths of the T-beam and pavement concrete, respectively;  $f_y$  and  $f_u$  are the yield and ultimate strengths of the longitudinal reinforcement, respectively; and  $E_s$  is the elasticity modulus of the main reinforcement.  $f_{GFRP}$  and  $E_{GFRP}$ , which are the ultimate strength and elasticity modulus of the GFRP, cannot be directly determined by engineering testing. The initial value of steel bars is adopted by the nominal value.

The original RS-OCT beam was exposed to a freeze–thaw cycle and humid environment for a long time, covered with dirt, initial microcracks, and defects, as shown in Figure 3. The necessary preparation was conducted prior to the experiment.

After the RS-OCT beam was transported to the laboratory and lifted onto the supports, accurately calibrating the position of the specimen was the most important step. Afterwards, the dirt on the surface of the specimen were removed and the initial cracks were clearly marked before testing. Next, a draw grid with 200-mm spacing on both sides of the T-beam web was used to measure the cracks during loading. The web was divided into four areas (area 1-1, 1-2, 1-3, and 1-4). Finally, the smooth face of the loading point is critical for the loading process, and the loading point on top of the flange and pavement were troweled using cement mortar.



**Figure 3.** Deflection on the specimen surface.

## 2.2. Experiment Setup

Figure 4 shows the experimental setup. The specimen was subsequently placed in a loading reaction frame. The loading point was set at the mid-span of the specimen. A 2000 kN vertical hydraulic jack was fixed at the center of the girder of the loading reaction frame, the bottom of which was connected to the 1000 kN load sensor, and the end of the sensor was connected to the loading plate pair and placed on the rigid distribution steel beam.



**Figure 4.** Experimental setup.

The rigid distribution beam was a 3-meter-long steel body. The pure bending zone was pre-designed as 2500 mm. The support of the rigid distribution beam was made of two rubber pads at each end of the rigid distribution beam (Figure 5a). The function of rigid distribution beam is establishing a beam section, which only bearing bending.

The support of the specimen consisted of upper rubber pads and lower rigid piers and was constrained by anchors on the floor (Figure 5b).

In addition, the safety and stability of RS-OCT beams were carefully ensured. Pairs of protective angle frames were anchored to the ground and placed on both sides of 1/3 and 2/3 spans of the specimen (Figure 5c).

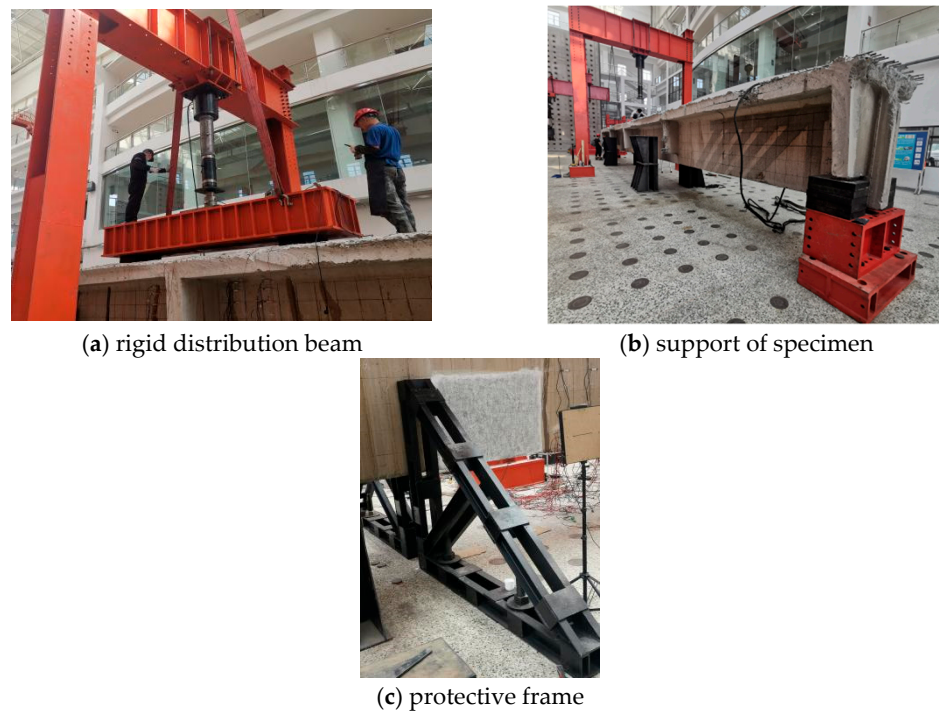


**Figure 5.** Detail of the experiment setup. (a) is the device of rigid distribution beam (b) present the state of specimen support, and (c) is triangular protective frame.

Five dial indicators were arranged under the bottom of the specimen at the midpoint, quartile points, and end of the span, as shown in Figure 6b. The strain gauges of the specimen were divided into three groups. Group I included three concrete strain gauges arranged in each row of pavement along the length of the specimen. The center point of the middle strain gauge corresponded to the mid-span section of the specimen, and the center distance of the strain gauges was 800 mm. In Group II, strain gauges were attached to the surface of the web on the two sides adjacent to the middle stiffening rib of the specimen, as shown in Figure 6c. The strain gages were arranged in four rows spaced 400 mm apart, with each row containing three strain gages spaced 150 mm apart. Group III included several 1 × 2 mm strain gauges to monitor the strain of the steel bar. Three rows of reinforced-bar strain gages spanning 800 mm were arranged on each web side. Strain gauges were attached to the inner reinforced bars by removing the protective concrete layer, as shown in Figure 6d.

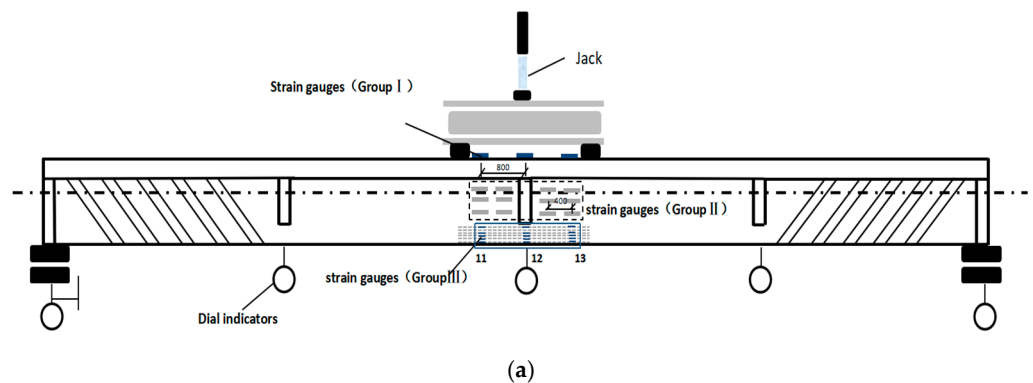


**Figure 6.** Cont.

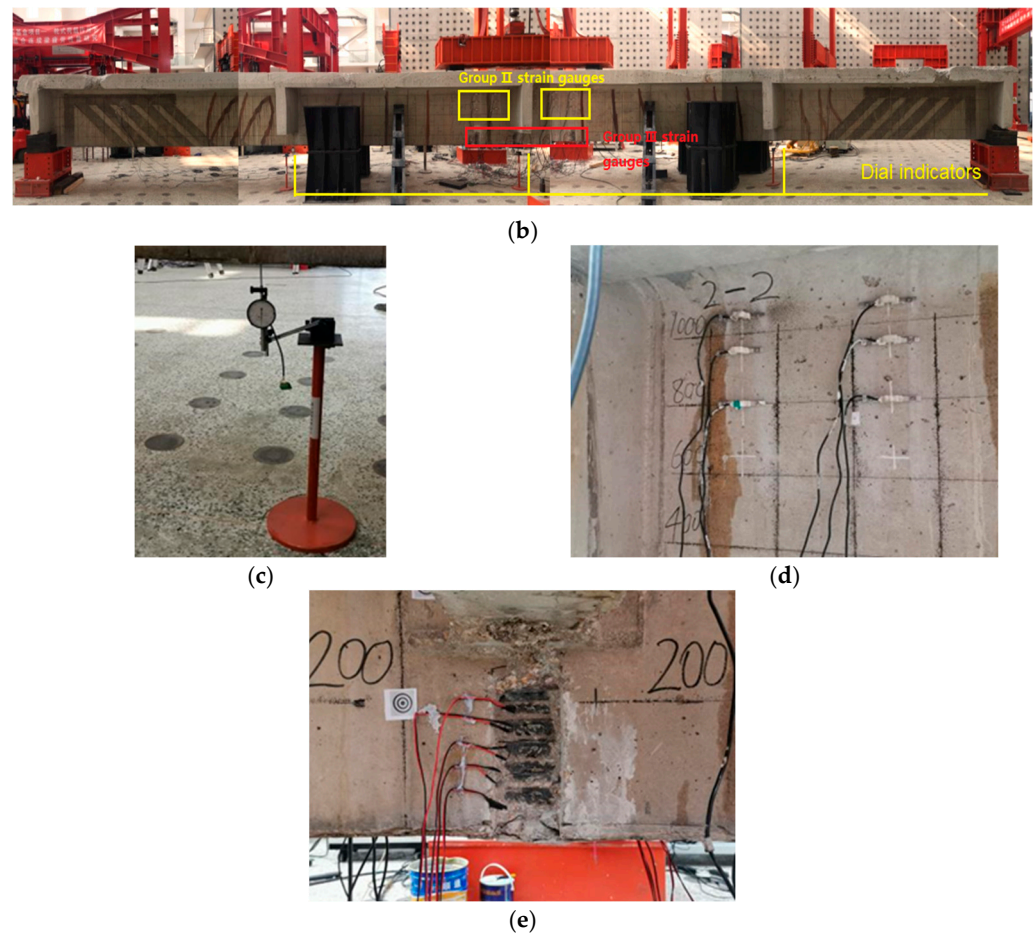


**Figure 6.** Detail of the dial indicators and strain gauges. (a,b) Dial indicators and strain gauges of specimen; (c) Dial indicator; (d) Strain gauges in Group II; (e) Strain gauges in Group III.

### 2.3. Experimental Process

The flexural experiments were carried out after the preparatory work was completed. Load control mode was adopted during loading. Figure 7a shows the distribution of the initial cracks in the specimen. The RS-OCT beam, which has been in service for more than 30 years, has a widely distributed crack. Most were retrofitted by pouring sealant, and others had microcracks less than 0.1 mm wide.

A first-grade load of 200 kN was applied to the specimen after preloading. As shown in Figure 7b, some initial cracks extended to a height of 500 mm, but a few microcracks appeared at the bottom of sections 1-2 and 1-3 of the web. The average height of the new cracks was nearly 200 mm with a width of 0.06–0.15 mm. The cracks continuously extended as the loading increased. When the load was 400 kN, most of the main cracks in sections 1-2 and 1-3 extended to a height of 400 mm. The largest crack reached 0.25 mm. In addition, cracks appeared on the surface of sections 1-1 and 1-4 under this load grade. Most of these cracks were distributed in the lower part of the web, with heights lower than 150 mm and widths smaller than 0.1 mm (Figure 7c). Additionally, 500 kN was the next grade load, as shown in Figure 7d, and new cracks appeared in sections 1-2 and 1-3. The height of the initial crack extension was small; however, the crack width increased. The largest width was 0.42 mm. In addition, more cracks appeared in sections 1-1 and 1-4. The largest crack in section 1-4 was approximately 600 mm from the bottom. In the grade of 500–600 kN, the overall deformation of the specimen increased. In this grade, rare new cracks appeared in many areas of the web, and some existing cracks in sections 1-2 and 1-3 connected and extended to the height of 800 mm, with the largest width of 0.48 mm, as shown in Figure 7e. The next grade was 700 kN, and the cracks continuously extended, as shown in Figure 7f.

The extent of crack propagation in sections 1-1 and 1-2 was lower than that in sections 1-3 and 1-4. An apparent crack appeared at the edges of the GFRP strips, with an average width of 0.7 mm. The cracks beside the rib plate at the mid-span rapidly connected, and the mid-span deflection of the specimen significantly increased.

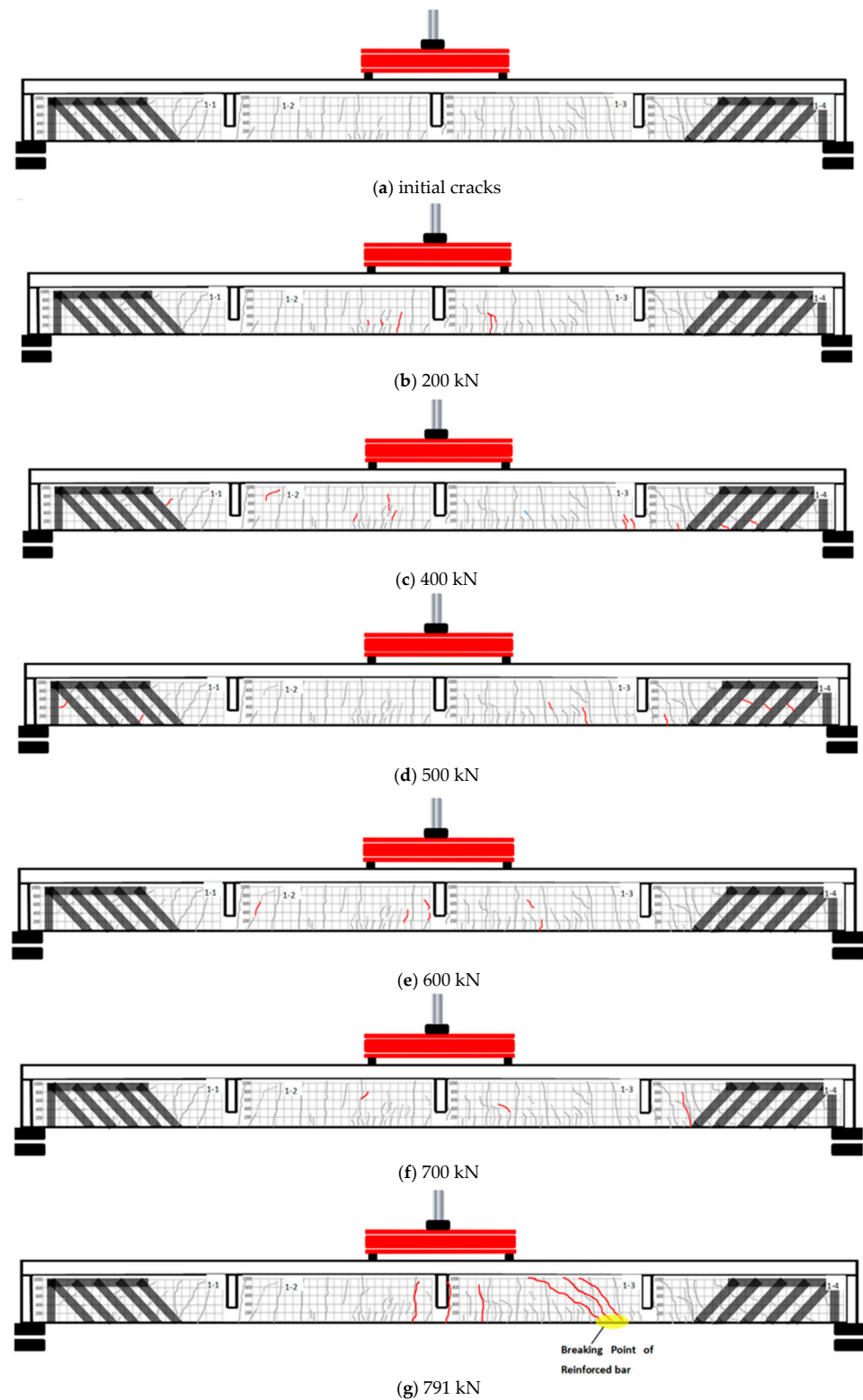


Figure 7. Cracks on the web of the specimen. (a) is the initial state or crack of specimen, and (b–g) present the crack state in different loading grade.

After the load reached 750 kN, the sound of the GFRP strips was clearly heard, and the deformation of the specimen rapidly increased. The main cracks can be clearly observed in sections 1-3 and 1-4, and the small cracks in section 1-3 of the web gradually expanded to connect with one another. There were multiple diagonal cracks from the bottom of the connecting partition board to the end of the loading distribution beam in sections 1-3 and 1-4. With an increase in the load, the cracks in section 1-3 rapidly connected. Three large oblique cracks formed through the web in section 1-3, and the largest crack width was 12 mm. The deformation of the specimen sharply increased, and consequently, debonding of the GFRP occurred.

When the load increased to 772 kN, the sound blared and the local GFRP strips attached to the bottom of the web suddenly debonded. When the load reached 791 kN, with a loud noise, a longitudinal reinforced bar at the bottom of section 1-3 broke, and the maximum crack width reached 15 mm. The bearing capacity of the specimen rapidly fell and was completely lost shortly after, as shown in Figure 7g.

## 2.4. Analysis of Experiment Results

### 2.4.1. Analysis of Ultimate State of the Specimen

After the experiments, the ultimate state of the specimen was carefully investigated. As expected, the entire deformation was characterized by the fovea of the middle span. However, the rupture of the longitudinal steel bars appeared not at the expected point exactly in the middle span, but at a distance of 3530 mm from the mid-span section, as shown in Figure 8.

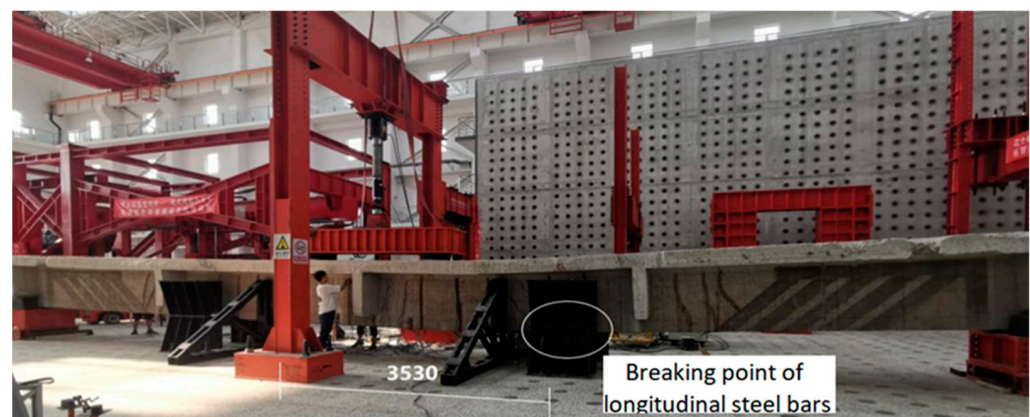


**Figure 8.** The ultimate state of the specimen.

After testing, anatomical manipulation was performed by removing the concrete protective layer at the failure point of the longitudinal steel bars. It is worth noting that the longitudinal rebars on both sides of the web snapped. Two 32 re-bars at section 1-3 and three 32 re-bars at the opposite section 2-3 were snapped from the bottom of the web, as shown in Figure 9a. However, the state of the cross-section of the reinforcement breaking point in the two sections was different. As shown in Figure 9b, the broken reinforcements in section 1-3 (two 32) are flat without the necking phenomenon. The broken reinforcement section (three 32) in section 2-3 was also flat; however, there was a weld joint on the middle reinforcements, as shown in Figure 9c. A steel bar with a weld joint was welded and fixed using two additional upper and lower bars. The cross-section of the welded reinforcement joint was severely corroded and nearly rusted. On the cross-section of the upper and lower reinforcements, the fracture section can be divided into semi-elliptical smooth and rough regions.

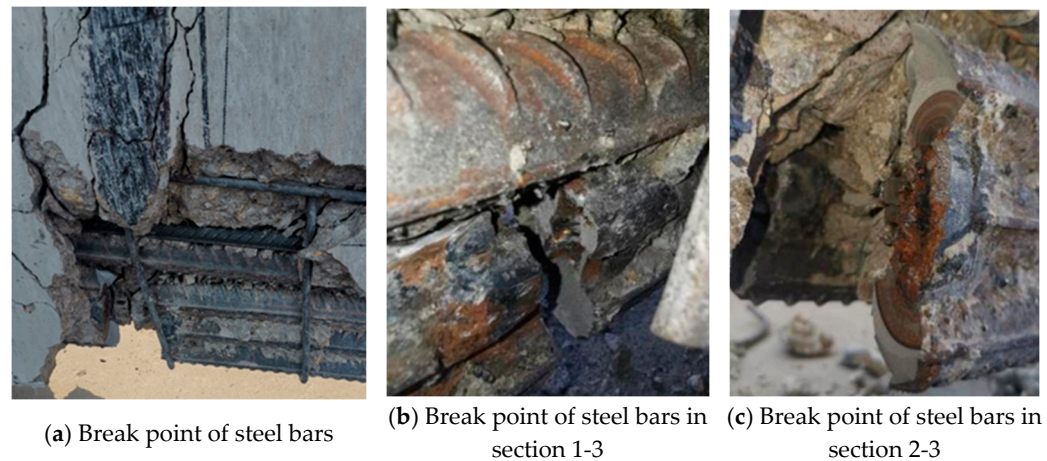


**Figure 9.** Break point of reinforced longitudinal bars. (a) is the detail of steel bar break point, (b) is the image of break point in section 1-3, (c) is the break point in section 2-3.

The morphological features of a fracture appear to be the classic state of steel subjected to a long-term fatigue load. Microcracks appeared in the weld joints long ago and propagated under cyclically repeated stress during service. The semi-elliptical smooth region can be attributed to the materials on both sides of the crack squeezing and separating from each other repeatedly. The continuous propagation of cracks gradually weakened the section, and the steel bars suddenly failed when the residual section was not sufficiently strong to resist the load. The rough region results from avulsion.

It can be inferred from this cross-section that microcracks existed in the reinforcement joint for a long period. Long-term water seepage led to the internal corrosion of solder joints. The welded reinforcements have nearly lost their effectiveness. The two adjacent longitudinal bars bore the long-term fatigue loads. Therefore, the welded joint was the weakest point in the entire specimen. Under a continuous test load, the weak spot suddenly lost its carrying capacity, and stress redistribution occurred immediately, leading to the fracture of the longitudinal reinforcement.

#### 2.4.2. Analysis of Bearing Capacity and Displacement

Figure 10 shows the load–displacement curves of the RS-OCT beam specimen. The ultimate bearing capacity of the specimen under flexural load is 791 kN, and the largest displacement in the middle point is 200 mm. The curve in Figure 10 can be divided into two parts: an ascending section and a strengthening section. The displacement in the middle span increased with load upgrading. The slope of the curve significantly decreased after approximately 700 kN, indicating that the displacement of the middle point rapidly increased after the loading level. The bearing capacity suddenly decreased at the end of the strengthening curve, fulfilling the characteristics of brittle failure.

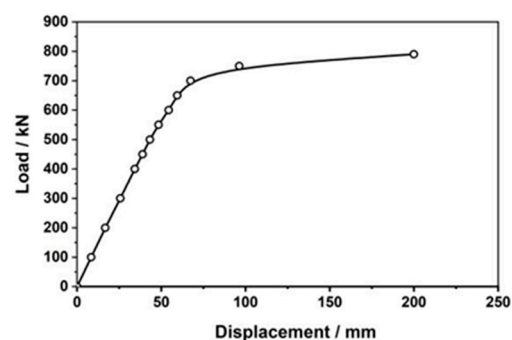


**Figure 10.** Load–displacement curve.

Figure 11 shows the displacement of the measurement points, including the end, quarter, and middle points, under loads at all levels. The loss of data of displacement under ultimate load level is due to the emergency removal of dial indicators at the final moment. The displacement at point 2 was larger than that at any of the other four points under the 100 kN load, as shown in Figure 11. For the location of point 2, corresponding to the rib between sections 1-3 and 1-4 in Figure 7, the aforementioned phenomenon can be explained by the initial deflection of the longitudinal bars. With the increase of the load, the displacement of point 3 in the middle span caught and overtook the displacement of point 2 between 200 and 300 kN. However, the displacement at point 2 was always greater than that at point 4. The expected symmetry could also be attributed to the deflection of the welded longitudinal reinforcement.

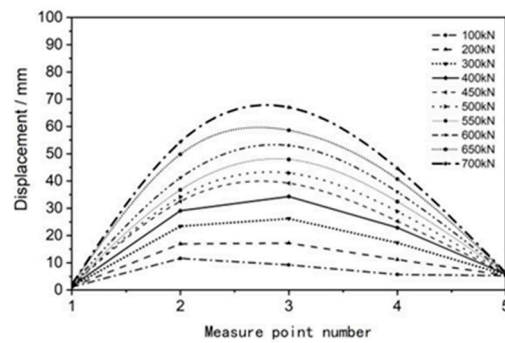


Figure 11. Displacement of measure point.

### 2.4.3. Analysis of Strain Distribution

#### Strain of Concrete

The strain gauges arranged on the concrete were divided into two groups: Group I on top of the flange and Group II under the flange, as shown in Figure 6a. The changes in the strain gauges in Group I are presented in Figure 12. In the figure,  $C_{xyz}$  represents the concrete strain gauge in  $x$  section,  $y$ th row, and  $z$ th line. It is evident that, as the load increased, the strain significantly increased. The strain gauge with the smallest strain change was C112 in the middle of the top gauges, and gauge C111 exhibited the largest value. This phenomenon resulted from the strengthening effect of the concrete rib in the middle span. The differences in the strain values of C111 and C113 can be attributed to the asymmetry of the RS-OCT beam. Figure 13 shows the strain distribution of C111-C141, and it indicates that the strain change in concrete fulfills the plate assumption during loading, especially before 400 kN loading. The latter slightly changed because of progressive cracking of the concrete surface.

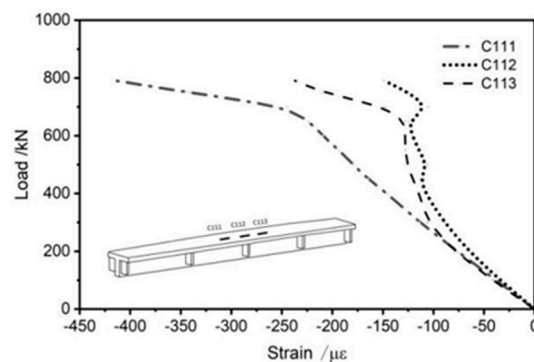


Figure 12. The strain gauges in Group I.

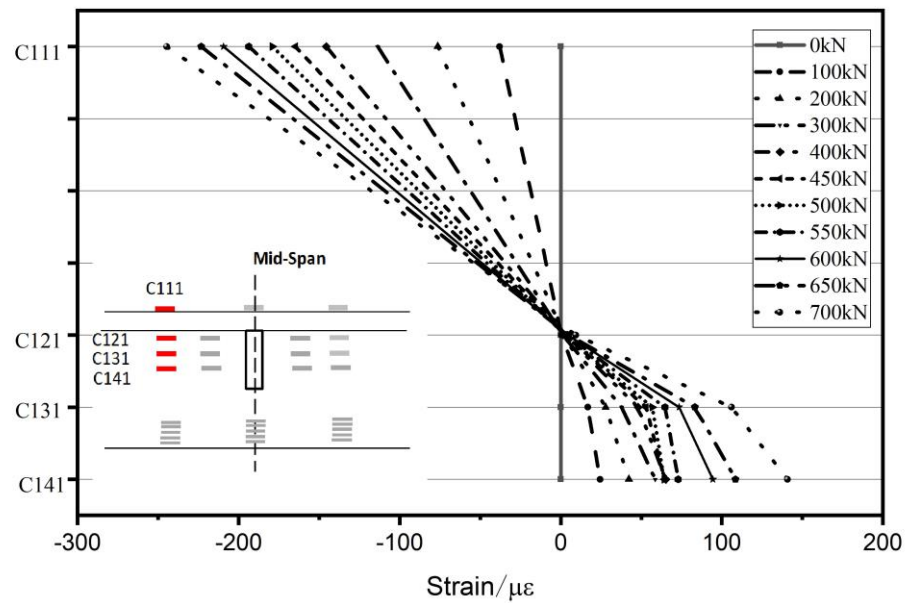


Figure 13. The strain gauges in Group II in line 11.

### Strain of Reinforcing Steel Bars

The strains of the reinforcing steel bar at all measured points are shown in Figure 14a–f. Measurement points 11, 12, and 13 are shown in Figure 6, and points 21, 22, and 23 indicate the counterpart points on the opposite face of the web. “Sxyz” presents the reinforcing steel bar strain gauge in *x* section, *y*th row, and *z*th line. It is evident that the strain distribution of the reinforcing steel bars on the two faces is irregular and disordered, indicating poor coordination of the inner longitudinal reinforcing steel bars. For the RS-OCT beam, the tensile reinforcement consisted of six longitudinal reinforcing steel bars in the flexural zone. In addition, in Figure 14a, the strain of one or two steel bars is lower than the others in each load level (as S141). A similar phenomenon is also exhibited in Figure 14b,e,f, which indicates the heterogeneous bond slip existing between the concrete and the longitudinal steel bars.

The location of the welded joint, cracks in the concrete, geometric position, and dimensions can influence the coordination work.

The strain distributions in the middle-span section of the RS-OCT beam based on the strains of the concrete and reinforcing steel bars are shown in Figure 15. In this figure, the sectional strain distribution of the steel bars does not strictly fulfill the plate assumption, which can be explained by the poor deformation coordination of the vertical bars. However, the overall strain distribution, including the concrete and steel bars, fulfilled the plate assumption.

### 2.5. Fatigue Life Testing of the Reinforced Steel Bar

As previously mentioned, the ultimate state of the RS-OCT beam in the test was unexpected, and the steel bars in the failure section exhibited obvious fatigue failure characteristics, as shown in Figure 9. Therefore, the fatigue properties of the longitudinal steel bars are vital to the behavior of RS-OCT beams. For an RS-OCT beam that is subjected to a cyclical vehicle load for a long period, the mechanical performance of the reinforcing steel bars under a fatigue load is critical. The fatigue life of a longitudinal steel bar must be known before the analysis. According to the test results of the RS-OCT beam, longitudinal steel bars can be classified into three groups: intact bars without damage, butt-weld bars with joints, and adjacent bars with welded damage. Subsequently, the corresponding test samples were simulated. A fatigue test was conducted, which indicated the fatigue life of the three types of steel bars. Three specimens, with a diameter of 32 mm and a length of 500 mm, were used, including one intact steel bar without a welded trail, one steel bar with

welded damage, and one connected steel bar with a weld joint. The test results are listed in Table 2. In Table 2, the intact steel bar has a fatigue cycle life of more than 2000 thousand times, whereas the steel bar with the welded joint has a minimum life span of 432 thousand times. A steel bar with welded damage has a cyclic life of 706 thousand times, indicating that the weld operation weakens the fatigue performance of the steel bar. The welded joint is the weakest point of the steel bars. This weakening effect must be considered for RS-OCT beams, as shown in Figure 16a,b.

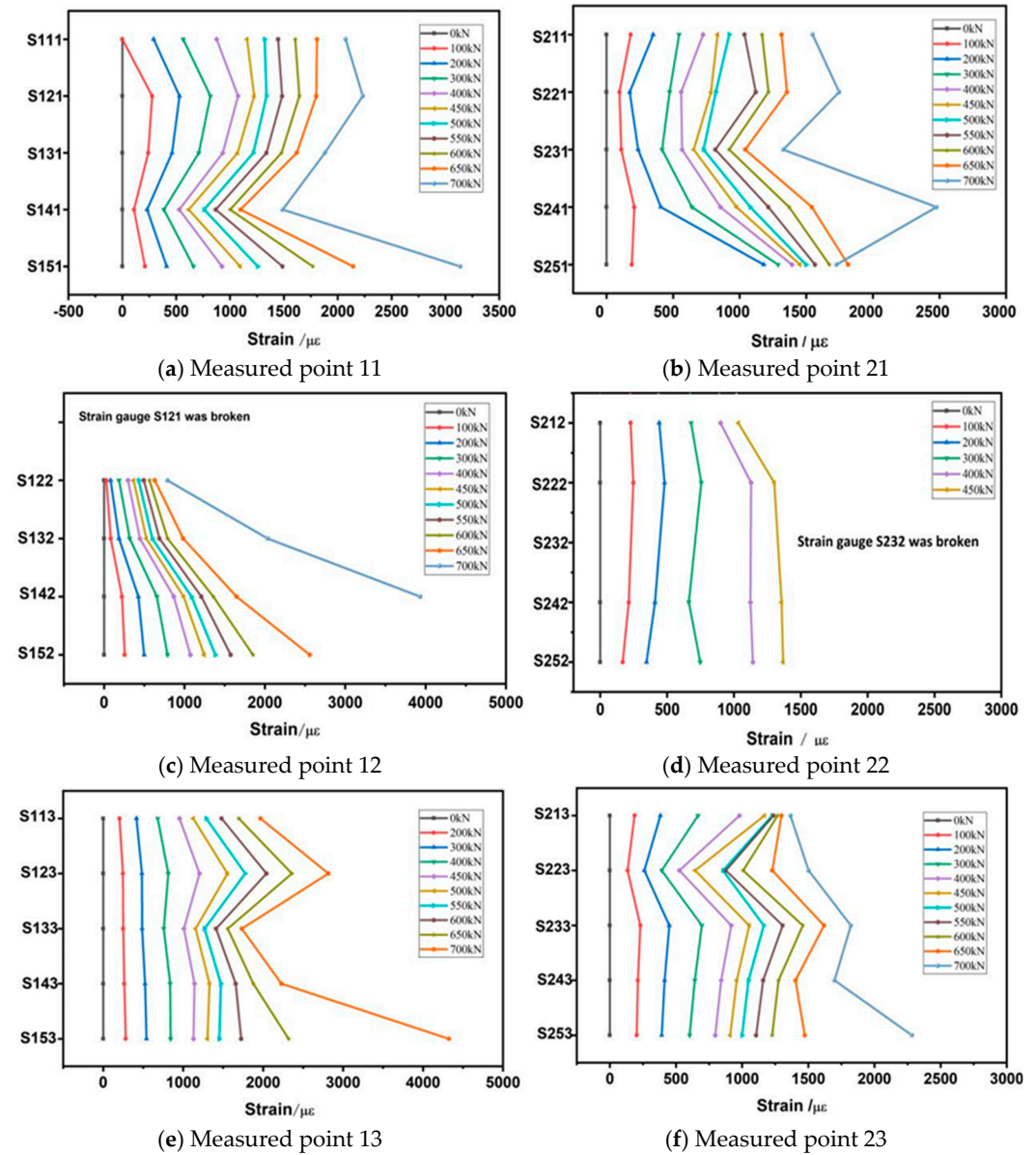


Figure 14. Strain of reinforcing bar in all measured points.

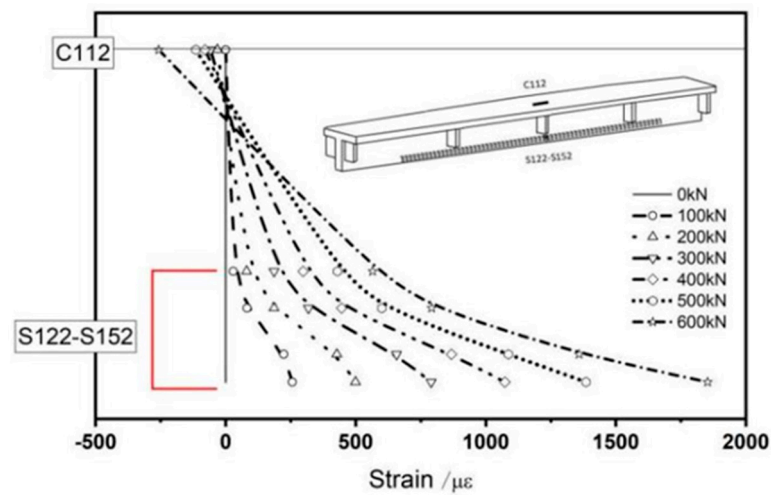


Figure 15. The sectional strain distribution.

Table 2. The result of the fatigue test of the steel bars.

Specimen	Situation	Fatigue Cycle Life (Thousand Times)	Final State
1	Intact steel bar	2000	Brittle fracture in middle length
2	Steel bar with welded joint	432	Brittle fracture in welded joint
3	Steel bar with welded damage	706	Brittle fracture in damage zone



(a) Cross-section of the steel bar without welding damage subjected to fatigue load



(b) Failure state of the steel bar with welded joint subjected to fatigue load

Figure 16. The fatigue test of the reinforcing steel bars.

### 3. Finite Element Analysis

Based on the experimental results, the RS-OCT beam specimen exhibited unexpected bending characteristics. For further research on the flexural behavior of the RS-OCT beam during service at any period, finite element analysis was carried out using the ABAQUS software.

#### 3.1. Establishing the Finite Element Model

A finite element model of the RS-OCT beam was built based on the practical situation of the specimen, by an implicit analysis module.

The dimensions and material properties were obtained from the measured values of the engineering inspection in Table 1, and these are shown in Figure 17. However, the

properties of GFRP cannot be obtained by practical testing for tight pasting. The properties of the GFRP and the layout of the inner reinforced bars were set based on the original design. The concrete was modeled using 3D solid continuum elements of brick, all with linear interpolation and normal Gauss integration. The average size of mesh was set to 175 mm, fulfilling the general recommendation of mesh dimension, larger than the biggest diameter of aggregate. Considering the convergency of mesh, the mesh sizes of longitudinal steel bars and GFRP are similar to the that of concrete.

For the large deformation of the specimen, 8-node reducing integration solid element (C3D8R) was adopted to simulate the beam, concrete pavement, and loading plate to avoid the locking effect during the calculation. The inner reinforced bars were simulated by a 2-node truss element (T3D2). The GFRP strips were simulated using 8-node membrane elements (M8R). The loading plate on the top of the beam was set as a rigid body, The loading plate was coupled to a load reference point, and a load (displacement) was applied to the load reference point, which was coupled with the loading plate. The contact between the steel bars and concrete was 'embedded', and the GFRP strip was tied to the body of the specimen.

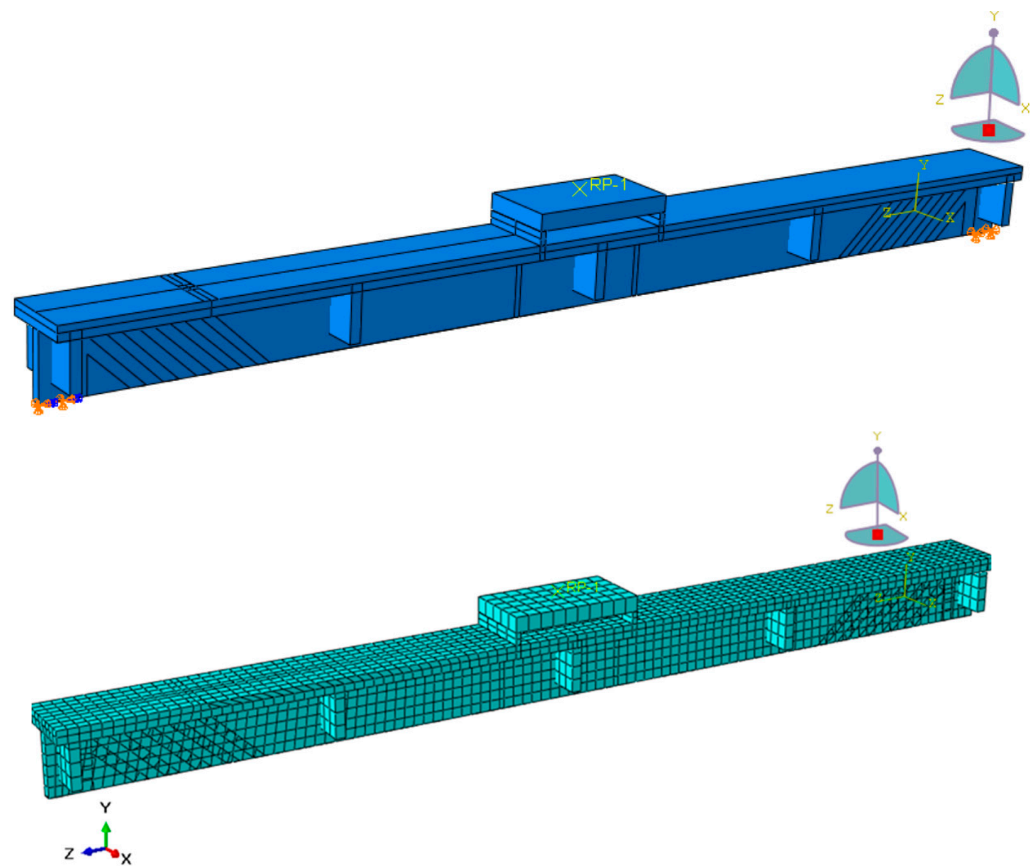


**Figure 17.** Finite element model of the RS-OCT beam.

The boundary condition of the specimen in FE analysis fulfilled the boundary condition of specimen in laboratory strictly. In FE analysis, the hinge on the two sides of the specimen was simulated by constraint with free rotation, as shown in Figure 17.

The loading condition of the specimen also fulfilled the state of experiment; static bending load was applied to the specimen, and the effect of fatigue accumulation was considered by the loss of material properties as follows.

### 3.2. Constitutive Model of the Material

#### 3.2.1. Compressive and Tension Behavior of Concrete

The plastic damage model was adopted to simulate the material properties of the concrete of the beam body and the pavement. The basic constitutive model of concrete materials adopted the model found in the Code for Design of Concrete Structures GB50010-2010 (2015 version) [19], as shown in Equations (1)–(7).

$$\sigma_{c(t)} = (1 - d_{c(t)})E_c\varepsilon \tag{1}$$

$$d_c = \begin{cases} 1 - \frac{\rho_c n}{n-1+x^n} & x \leq 1 \\ 1 - \frac{\rho_c}{\alpha_c(x-1)^2+x} & x > 1 \end{cases} \tag{2}$$

$$d_t = \begin{cases} 1 - \rho_t[1.2 - 0.2x^5] & x \leq 1 \\ 1 - \frac{\rho_t}{\alpha_t(x-1)^{1.7}+x} & x > 1 \end{cases} \tag{3}$$

$$E_c = 4750\sqrt{f_c} \tag{4}$$

$$\rho_{c(t)} = \frac{f_{c(t),r}}{E_c\varepsilon_{c(t),r}} \tag{5}$$

$$n = \frac{E_c\varepsilon_{c,r}}{E_c\varepsilon_{c,r} - f_{c,r}} \tag{6}$$

$$x = \frac{\varepsilon}{\varepsilon_{c(t),r}} \tag{7}$$

where  $E_c$  presents the elastic modulus of concrete, related to the ultimate strength of concrete  $f_c'$ , which can be calculated according to Equation (4).  $\varepsilon$  presents the strain of concrete.  $d_{c,t}$  is called the damage index under compressive and tension behavior, which are determined by Equations (2) and (3), respectively. In Equations (2) and (3),  $\alpha_c$  and  $\alpha_t$  are called descending coefficients. In Equation (5)  $f_{c(t),r}$  and  $\varepsilon_{c(t),r}$  are the compressive and tension strength and corresponding strain of peak point on the constitutive curve of concrete, respectively. The ultimate compressive strain of concrete can be obtained from the table in GB50010. The specific interpretation of parameters in Equations (1)–(7) refers to GB50010. The damage of concrete must be considered for the concrete beams suffering fatigue load. The cyclic damage model, considering the stiffness degradation of concrete, was adopted in this study [20].

#### 3.2.2. Tension Behavior of Reinforced Steel Bars

According to the related experiment, the constitutive curve of reinforced steel bars can be simplified by the harden bi-linear curve, in which the elastic modulus  $E_s$ , yields strength  $\sigma_y$ , and ultimate strength  $\sigma_u$  of steel bars are necessary.

#### 3.2.3. Tension Behavior of the GFRP

The GFRP attached to the surface of the specimen was regarded as an elastic material during loading. The constitutive law was determined by the elastic modulus and ultimate tensile strength of the material. Figure 18 shows the constitutive law of the material used in finite element analysis.

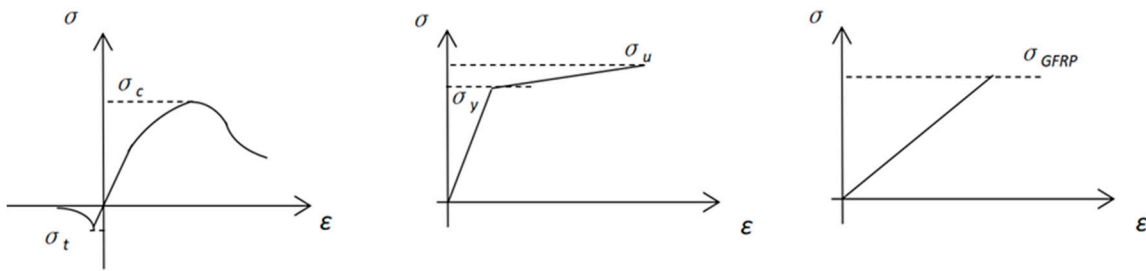


Figure 18. Constitutive curve of material.

### 3.3. Simulation of the Welded Deteriorated Zone of the Steel Bar

In this study, the unexpected ultimate failure pattern of the RS-OCT specimen stems from the weak welded joints. The weakly deteriorated zone can be considered as a composite system of the welded point and the welding thermal damage zone on the adjacent steel bars, as shown in Figure 9c.

Based on the aforementioned fatigue tests of the steel bars, the fatigue lives of the intact steel bars, steel bars with welded damage, and steel bars with butt-welded joints are different. Therefore, a weakly welded zone can be simulated using the constitutive relation of the fatigue performance. According to the experimental results, the distributed length of the thermal damage zone on the upper and lower reinforced bars was approximately 10–20 mm, and the middle-welded steel bar nearly broke off before the bending load was applied.

The damage to the related steel bars can be simulated by reducing the effective area of the cross-section, which is commonly used in the related literature [21]. The method is based on the theory of Miner’s rule, called “Cumulative damage of reinforcement”. The basic expression of the theory is shown as Equation (8) [22]. The theory was adopted by many other studies [23,24].

$$D_s = \sum \frac{n_i}{N_i} \tag{8}$$

where  $D_s$  is accumulation of fatigue damage,  $n_i$  is the cyclic number for the specified stress amplitude of tensile steel bars, and  $N_i$  is the cyclic number to failure for the stress amplitude of tensile steel bars.

The equivalent area of the reinforced bars subjected to a fatigue load can be determined using Equation (9).

$$A_s^f(N) = A_s \left[ 1 - \frac{N}{N_f} \left( 1 - \frac{\sigma_{\max}(N_f)}{f_y} \right) \right] \tag{9}$$

In addition, the relationship can be expressed as a pattern of the equivalent residual strength as follows:

$$f_y(N) = (\sigma_{\min} + \Delta\sigma) \left[ 1 - \frac{N}{N_f} \left( 1 - \frac{\Delta\sigma + \sigma_{\min}}{f_y} \right) \right] \tag{10}$$

in which  $1 - \frac{N}{N_f} \left( 1 - \frac{\sigma_{\max}(N_f)}{f_y} \right)$ , usually defined as  $D(N)$ , refers to the damage index of reinforced bars.  $N$  and  $N_f$  are the number of cyclic fatigue and the fatigue life of steel bars, respectively.  $\sigma_{\max}(N_f)$  presents the maximum stress during fatigue life, which can be determined by the minimum stress  $\sigma_{\min}$  and the fatigue stress radiation  $\Delta\sigma$ .  $A_s$  and  $A_s^f(N)$  refer to the initial area of reinforced bar and the equivalent area of reinforced bar after  $N$  times cyclic load, respectively.

### 3.4. Verification of the Finite Element Model

The load–displacement curves of the RS-OCT beam in the middle-span section of the finite element analysis and the experimental results are compared in Figure 19. The FEA curve agrees with the experimental results. Notably, in the initial stage (before yielding), the

two curves had large distances, which might mainly be attributed to ignoring the slipping of the inner steel bars and many other factors such as measured error of equipment.

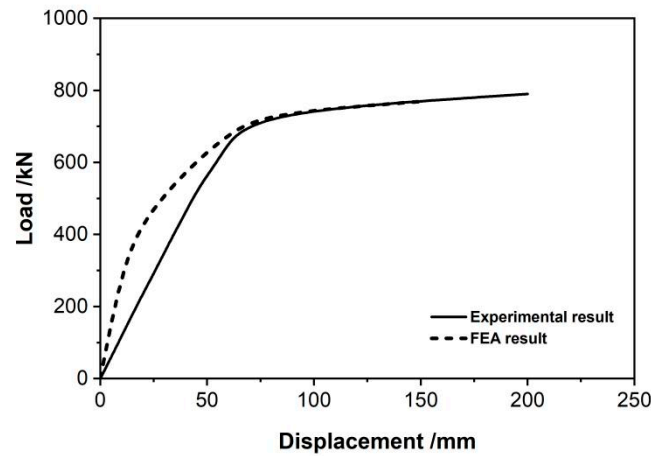


Figure 19. Comparison of the FEA and experimental curves.

The ultimate state of the finite element analysis results in Figure 20 correspond to the experimental results in Figure 8. The deformations of the specimen are asymmetrical. The strain of the right lateral bar was larger than that of the other lateral bars, and the strain was also larger than that of the other longitudinal bars for the weak zone of the longitudinal reinforced bars.

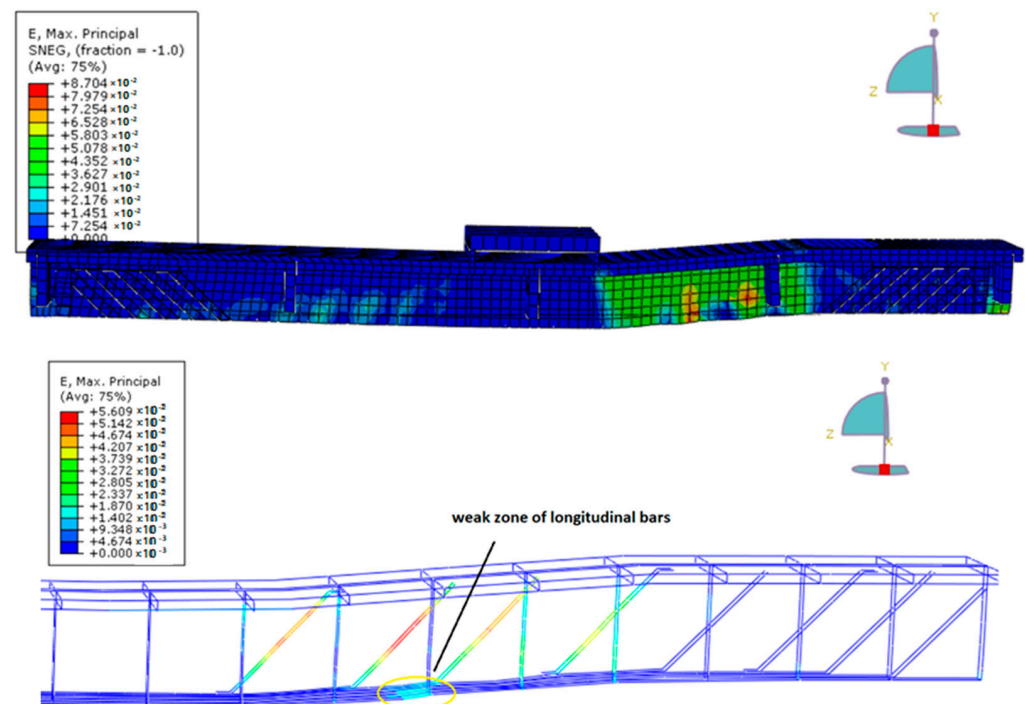


Figure 20. Strain of the concrete and the inner steel bars.

#### 4. Analysis of Influencing Factors on the Bearing Capacity of the RS-OCT Beam

##### 4.1. Influence of Deteriorated Longitudinal Steel Bars

Based on Section 3.3, longitudinal reinforced bars, including intact steel bars, steel bars with butt-welded joints, and steel bars with welded damage, have different fatigue lives under various stress levels. Compared to the specimen with intact reinforced bars, the

flexural bearing capacity of the RS-OCT beam with deteriorated reinforcement is lower in most situations.

Figure 21 presents the load–displacement curves of various specimens with common deterioration ratios at different deterioration locations. In the figure, the flexural bearing capacity of the specimen decreases as the distance from the deteriorated region to the mid-span decreases, indicating that the bearing capacity of the RS-OCT beam is closely related to the location of the deteriorated region on the longitudinal steel bars. Figure 22 shows the comparison of load–displacement curves of the specimens with a common location (mid-span) but different deteriorated ratios. The deterioration ratio is defined as the ratio of the sectional area of deteriorated steel bars to that of the intact steel bars. It can be inferred that the bearing capacity of the specimens with a common deterioration location decreased as the deterioration ratios increases.

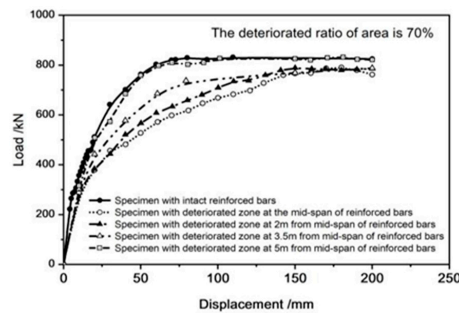


Figure 21. The curves of specimens with different deteriorated locations.

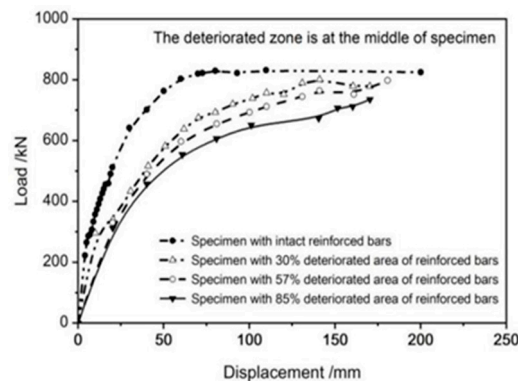


Figure 22. The curves of specimens with different deteriorated ratio of steel bars.

#### 4.2. Influence of Atmospheric Environment

##### 4.2.1. Compressive Strength of Concrete

The compressive strength changes with service time, especially for structures exposed to the atmospheric environment for a long time. This phenomenon has been observed in several studies [25,26].

The RS-OCT beam in this study has been in service in a general air environment for a long period. The variation law of concrete strength can be expressed using the Yue (2023) model [26].

$$\mu_f(t) = \eta(t)\mu_{f0} \tag{11}$$

$$\eta(t) = -2.4 \times 10^{-4}t^2 + 0.01t + 1.3 \tag{12}$$

where  $\mu_f(t)$  is the average value of concrete strength after a long time of service, and  $\eta(t)$  is the variation index, which is related to the service life  $t$ /year.

### 4.2.2. Tension Strength of Steel Bar

The performance of the steel bar also deteriorates due to environmental erosion during long-term service. The amount of quality loss can be calculated using the classic model of Niu (1997) [27], which is given by Equations (12)–(17).

$$W_t = \begin{cases} 2.35P_{RA}D_0\frac{R}{K_c^2}[\sqrt{R^2 - (R + c - K_c\sqrt{t})^2} - (R + c - K_c\sqrt{t})\arccos\frac{R+c-K_c\sqrt{t}}{R}] & (t_p \leq t \leq t_{cr}) \\ W_{cr} + 1.173P_{RA}D_0(t - t_{cr}) & (t > t_{cr}) \end{cases} \quad (13)$$

where  $P_{RA} = 0.787$ .  $D_0$  is the osmotic coefficient and is determined by Equation (18).  $R$  and  $c$  are the radius of the longitudinal steel bar and the thickness of the protective layer, respectively, and  $x_0$  is equals 25. The relative index  $K_c$  can be calculated using Equation (16).  $f_{cuk}$  is the standard value of the concrete compressive strength.

$$W_{cr} = 1.204R(1 + \frac{c}{R})^{0.85} \times 10^{-3} \quad (14)$$

$$t_p = (\frac{c_a}{K_c})^2 \quad (15)$$

$$c_a = c + x_0 \quad (16)$$

$$K_c = \frac{24.48}{\sqrt{f_{cu,k}}} - 2.74 \quad (17)$$

$$D_0 = (\frac{32.15}{f_{cuk}} - 0.44) \times 10^{-2} \quad (18)$$

### 4.3. Influence of Cyclic Fatigue Action Strength of Concrete

Several studies have focused on the fatigue properties of concrete [28–31]. In this study, the variation law of concrete strength resulting from fatigue can be calculated using the model of Zhu (2012) [21], which is suitable for concrete bearing a fatigue load for a long time. The model of the variation law for the compressive behavior of concrete can be determined by Equations (19)–(22). The variation law of elastic modulus can be expressed in Equation (22) [28].

$$\sigma_r(N) = f_c \left( \frac{\frac{N}{N_f}[x(N_f) - x(1)]}{\alpha_d(\frac{N}{N_f}[x(N_f) - x(1)] - 1)^2 + \frac{N}{N_f}[x(N_f) - x(1)]} \right) \quad (19)$$

$$x(N) = \begin{cases} 1 & N = 1 \\ \frac{\lg N}{\lg N_f}[x(N_f) - 1] + 1 & 1 \leq N \leq N_f \end{cases} \quad (20)$$

$$x(N_f) = \frac{2\alpha_d\sigma_{\max} + f_c - \sigma_{\max} \pm \sqrt{(f_c - \sigma_{\max})^2 + 4\alpha_d\sigma_{\max}(f_c - \sigma_{\max})}}{2\alpha_d\sigma_{\max}} \quad (21)$$

$$E_N = (1 - 0.33N/N_f)E_0 \quad (22)$$

where the fatigue life of concrete is represented by the model of Hsu (1981) [29], as shown in Equations (23) and (24).

$$\frac{\sigma_{\max}}{f_c'} = 1 - 0.00662(1 - 0.566R)\lg N_f - 0.0294\lg T(\text{for short period}) \quad (23)$$

$$\frac{\sigma_{\max}}{f'_c} = 1.2 - 0.2R - 0.133(1 - 0.779R)\lg N_f - 0.05301(1 - 0.445R)\lg T \text{ (for long period)} \tag{24}$$

where  $\sigma_r(N)$  and  $\sigma_t(N)$  refer to the residual compressive strength of concrete.  $N$  and  $N_f$  are the fatigue time and the fatigue life of material, respectively.  $N_f$  of concrete can be determined by Equations (23) and (24).  $x(N)$  and  $x(N_f)$  can be obtained by Equations (20) and (21), respectively.  $E_0$  and  $E_N$  are the initial elastic modulus and former elastic modulus after  $N$  times fatigue load, respectively.  $f_c$  and  $f_t$  are the compressive and tension strength of concrete, respectively.  $\sigma_{\max}$  is the maximum stress of concrete under the maximum load, which can be determined by the section analysis, based on plat sectional assumption.  $\alpha_d$  is the parameter of concrete, which can be obtained from the design code of China.  $T$  is the service period. When the tension effect of concrete is very small, the loss of tension stress of concrete can be ignored.

The tension yield strength of the steel bars weakened by fatigue can be calculated using Equations (9) and (10). The fatigue life  $N_f$  of various steel bars was determined using the aforementioned fatigue test. The  $\sigma_{\min}$  is the stress of longitudinal bars under the minimum load (general pointing to the action of gravity).

Based on the aforementioned models, a typical value for the material was calculated, as shown in Table 3.

**Table 3.** The properties value of concrete and steel bars.

	Concrete Strength under the Action of Atmospheric Environment/MPa	Concrete Strength under the Action of Fatigue /MPa	Equivalent Diameter of Steel Bar under the Action of Environmental Erosion/mm	Equivalent Diameter of Steel Bar under the Action of Fatigue /mm
initial value	22.4	22.4	32.0	32.0
5 years old	30.11	22.26	31.81	31.82
10 years old	30.82	22.25	31.69	31.65
15 years old (Retrofitted)	31.27/ 42.3 (pavement)	21.28/ 42.3 (pavement)	31.57	31.48
20 years old	31.45/ 56.85 (pavement)	21.27/ 42.2 (pavement)	31.46	31.28
25 years old	31.36/ 58.2 (pavement)	21.26/ 42.1 (pavement)	31.33	31.10
30 years old	31.00/ 59.05 (pavement)	21.25/ 42.1 (pavement)	31.21	30.92
33 years old (Nowadays)	30.65/ 59.31 (pavement)	21.25/ 42.1 (pavement)	31.19	30.82

According to the theory of time-dependent concrete compressive strength and concrete fatigue, the atmospheric environment and fatigue are the dominant factors affecting the strength of concrete and equivalent diameter of reinforced bars. The influence of individual factors is shown in Figure 23a,b.

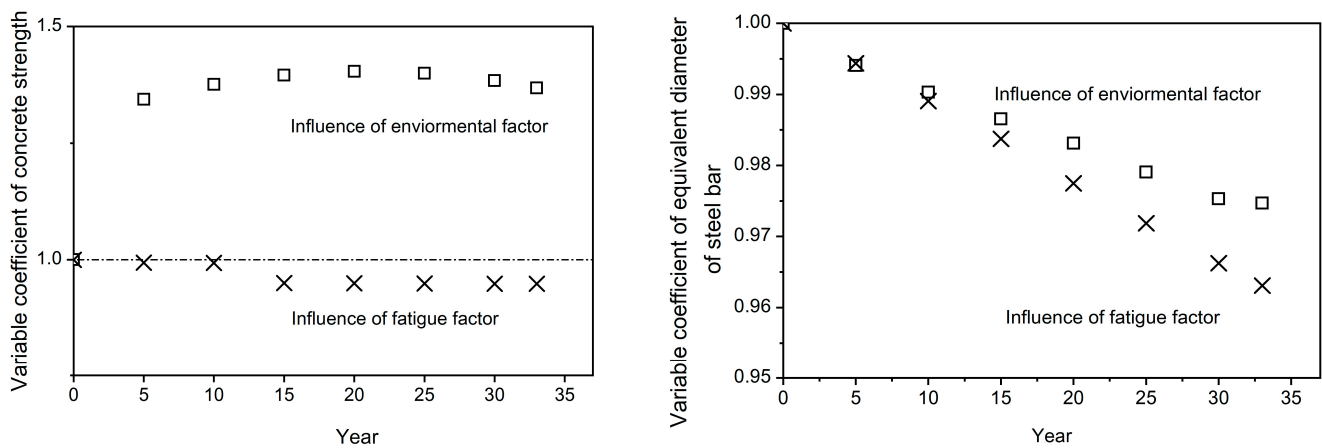


Figure 23. Variable coefficient of concrete and equivalent diameter.

4.4. Combination Index of the Two Factors

The influence indices of fatigue and atmospheric environment can be expressed as  $F(t)$  and  $E(t)$ , which are related to the number of fatigue cycles and service years, respectively. The performance of the steel bar continued to change with the service year and frequency of cyclic loading. The decrease in the steel bar performance can be expressed by reducing the equivalent diameter. The compressive strength of the concrete and the equivalent diameter of the steel bars of the RS-OCT beam subjected to a long-term fatigue load can be expressed as  $f_{cN}$  and  $D_{cN}$  in Equations (25) and (26), respectively.

$$f_{cN} = f_c \cdot \eta_c \cdot F(t) \cdot E(t) \tag{25}$$

$$D_{cN} = d_s \cdot \eta_s \cdot F(t) \cdot E(t) \tag{26}$$

The value of  $\eta$  can be calculated using the theoretical value presented in Table 3, and the measured value in Table 1 is for the concrete of the beam body and pavement. A regular pattern can be observed: before 20 years, the value of  $\eta_c$  is approximately 0.83, and the  $\eta_c$  equals 1.07 after 20 years. This means that, before 20 years, the combined effect of the environment and fatigue was smaller than the addition of any independent effects. However, a larger effect must be considered when the service age is greater than 20 years. According to the value in the document and the measured value, the relative index of the steel bar  $\eta_s$  is equal to 0.85.

5. Analysis of the State of the RS-OCT Beam during Its Whole Life

5.1. Safety Reserving of the RS-OCT Beam

The safety state of the RS-OCT beam of a bridge can be evaluated using the safety reserving parameter, called “SR”, which is defined as the ratio of assistant force to design value. During the entire service life of the RS-OCT beam, the load borne by the specimen changed with the upgrading of the load standard, and the properties of the material continuously changed. According to previous studies, the main factors affecting the performance of the RS-OCT beam include environmental erosion and the cyclic load source from the vehicle. Based on the combination index obtained from the practice value, the material changes with the service term, as shown in Figure 24.

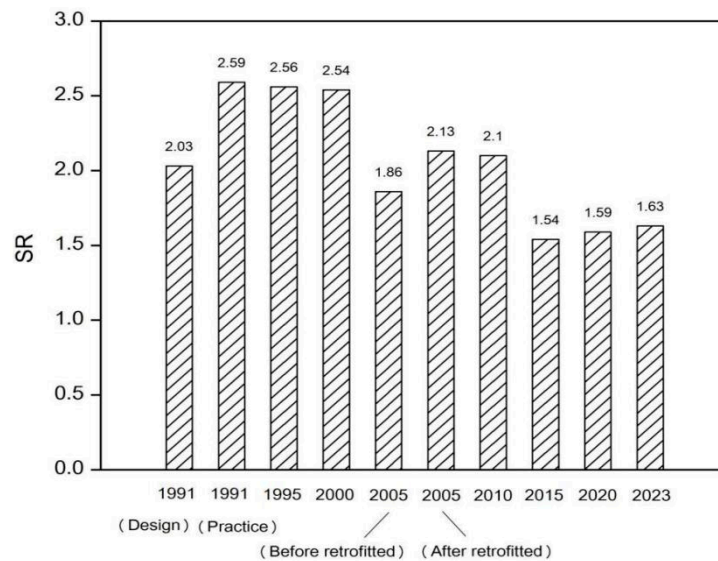


**Figure 24.** The variation of SR index of an RS-OCT beam with service time.

The flexural bearing capacity of the RS-OCT beam during its entire life span was calculated by finite element analysis using ABAQUS. It was confirmed that the performance of the material changed with service state. The SR is listed in Figure 24.

The SR parameter constantly changes. In 1991, the designed SR was 2.03. The actual value is 2.59, which is approximately 1.27 times higher than the design value, indicating that the design scheme is conservative. With the use of the RS-OCT beam, the trend in the SR value was stable before 2000 and dropped slightly. This phenomenon can be explained by the combined effect of a modest increase in the concrete compressive strength and a slight reduction in the yield strength of the longitudinal steel bars. The SR dropped to 1.86 in 2005, mainly resulting from the upgrading of the loading standard [32]. After retrofitting, the SR increased to 2.13 once more, presenting the necessity and significance of retrofitting. In the next five years after retrofitting, the SR was stable. In 2015, a sudden decline was observed. At this stage, upgrading the loading standard played an important role, although the concrete compressive strength of the pavement significantly increased. In fact, the safety reservation index had the lowest value of only 1.54. From 2015 to present, the SR has shown a slightly increasing trend, which can be explained by the increase in the compressive strength of pavement concrete with 18 years of age.

### 5.2. Discussion on the Limitations of the Proposed Method

As mentioned above, the proposed method for predicting the SR index is related to the service state of the RS-OCT beam. The proposed method was built on the basis of the verified finite element model and considering the comprehensive influence factors, such as fatigue action and atmospheric environment, studied by the previous research. The robustness of the study depends on the accuracy of the model and the universality of research results in the literature. Therefore, the limitations of the proposed method must be noted. Firstly, the RS-OCT beam in this study is a unique specimen. A database should be supplied in subsequent study. Secondly, the available literature related to the study of the influence of fatigue and environment on the performance of an RC specimen were mainly focused on the 2000s–2010s. Few new studies appeared in recent years, which limits the applicability of the model. The proposed method for predicting the SR index of an RS-OCT beam should be constantly improved.

## 6. Conclusions

The conclusions of this study are as follows:

(1) For RS-OCT beams, the longitudinal reinforced bars used to be connected through butt welding. The joint is a vulnerable spot that can result in premature failure. The

possibility of premature failure is related to the butt-welding quality and location of the butt-welding joint. For RS-OCT beams, the butt-welding joint should be replaced by a threaded sleeve joint.

(2) The RS-OCT beam maintaining a long-term effective flexural bearing capacity is mainly attributed to the special layout of the tightly packed vertical reinforcements. The vulnerable joint of the longitudinal bar is not individual; rather, the vulnerable joint on the longitudinal steel bars is an independent point and a deteriorated region.

(3) The RS-OCT beam is simultaneously subjected to environmental erosion and fatigue. Thus, the combination function can be determined as the product pattern of the influence indices. Parameter  $\eta$  can be inferred from the experimental results. For concrete, the value is larger than 1.0 after a service life of 20 years, but it is smaller than 1.0 before a 20-year service life. The value for the steel bars was approximately 0.85.

(4) The bearing state of the RS-OCT beam changed with the upgrade in the loading standard and retrofitting scheme. Upgrading the loading level played a dominant role in the change in the SR index. For the RS-OCT beam, the lowest safety reservations were observed in 2015.

**Author Contributions:** Conceptualization, T.H.; methodology, D.H.; formal analysis, L.W.; investigation, D.H.; resources, G.Z.; original draft preparation, D.H.; project administration, F.J. All authors have read and agreed to the published version of the manuscript.

**Funding:** This research received no external funding.

**Institutional Review Board Statement:** Not applicable.

**Informed Consent Statement:** Not applicable.

**Data Availability Statement:** Data is unavailable due to privacy.

**Conflicts of Interest:** The authors declare no conflict of interest.

## References

- Hou, D.; Hu, T.; Zhang, G. Experimental and Finite Element Study on the Shear Performance of Existing Super-Span Concrete T-Beams Retrofitted with Glass Fiber-Reinforced Plastic. *Sustainability* **2023**, *15*, 2768. [[CrossRef](#)]
- Nayak, C.B.; Narule, G.N.; Surwase, H.R. Structural and cracking behaviour of RC T-beams strengthened with BFRP sheets by experimental and analytical investigation. *J. King Saud Univ. Eng. Sci.* **2022**, *34*, 398–405. [[CrossRef](#)]
- Christophe Deniaud, J.J.; Cheng, R. Shear Behavior of Reinforced Concrete T-Beams with Externally Bonded Fiber-Reinforced Polymer Sheets. *ACI Struct. J.* **2001**, *98*, 386–394.
- Deifalla, A.; Awad, A.; Seleem, H.; Abdelrahman, A. Investigating the behavior of lightweight foamed concrete T-beams under torsion, shear, and flexure. *Eng. Struct.* **2020**, *219*, 11074. [[CrossRef](#)]
- Al Shboul, K.W.; Raheem, M.M.; Rasheed, H.A. Debonding characterization for all-lightweight RC T-Beams strengthened in flexure with FRP. *J. Build. Eng.* **2021**, *44*, 103377. [[CrossRef](#)]
- Zaki, M.A.; Rasheed, H.A.; Roukerd, R.R.; Raheem, M. Performance of reinforced concrete T beams strengthened with flexural CFRP sheets and secured using CFRP splay anchors. *Eng. Struct.* **2020**, *210*, 110304. [[CrossRef](#)]
- Zhang, J.; Xu, Y.; Mai, Z.; Lv, W. Flexural performance of RC T-beams strengthened with external double steel channel. *J. Build. Eng.* **2021**, *42*, 102453. [[CrossRef](#)]
- Haryanto, Y.; Hsiao, F.-P.; Han, A.; Chua, A.; Salim, F.; Nugroho, L. Structural behavior of negative moment region NSM-CFRP strengthened RC T-beams with various embedment depth under monotonic and cyclic loading. *Compos. Struct.* **2022**, *301*, 116214. [[CrossRef](#)]
- Zhang, Y.; Elsayed, M.; Zhang, L.V.; Nehdi, M.L. Flexural behavior of reinforced concrete T-section beams strengthened by NSM FRP bars. *Eng. Struct.* **2021**, *233*, 1119229. [[CrossRef](#)]
- Rahim, A.A.F.; Mohammed, A.A.; Al-Kamaki, Y.S.S. Flexural behavior of composite T-beam made of plastic waste aggregate concrete web and high-strength concrete flange. *Structures* **2023**, *47*, 2138–2147. [[CrossRef](#)]
- Hason, M.M.; Mussa, M.H.; Abdulhadi, A.M. Flexural ductility performance of hybrid-recycled aggregate reinforced concrete T-beam. *Mater. Today Proc.* **2021**, *46*, 682–688. [[CrossRef](#)]
- Farghal, O.A. Fatigue behavior of RC T-beams strengthened in shear with CFRP sheets. *Ain Shams Eng. J.* **2014**, *5*, 667–680. [[CrossRef](#)]
- Dong, Y.; Ansari, F.; Karbhari, V.M. Fatigue performance of reinforced concrete beams with externally bonded CFRP reinforcement. *Struct. Infratruct. Eng.* **2011**, *7*, 229–241. [[CrossRef](#)]

14. Al-Rousan, R.; Issa, M. Fatigue performance of reinforced concrete beams strengthened with CFRP sheets. *Constr. Build. Mater.* **2011**, *25*, 3520–3529. [[CrossRef](#)]
15. Li, X. Experimental Study on Fatigue Performance of Existing 8m RC T-girder of Heavy-Haul Railway. Master's Thesis, Shijiazhuang Tiedao University, Shijiazhuang, China, 2020.
16. Kim, J.K.; Kim, Y.Y. Experimental study of the fatigue behavior of high strength concrete. *Cem. Concr. Res.* **1996**, *26*, 1513–1523. [[CrossRef](#)]
17. Medeiros, A.; Zhang, X.; Ruiz, G.; Yu, R.C.; Velasco, M.d.S.L. Effect of the loading frequency on the compressive fatigue behavior of plain and fiber reinforced concrete. *Int. J. Fatigue* **2014**, *70*, 342–350. [[CrossRef](#)]
18. Ma, Y.; Wang, Q.; Guo, Z.; Wang, G.; Wang, L.; Zhang, J. Static and fatigue behavior investigation of artificial notched steel reinforcement. *Materials* **2017**, *10*, 532. [[CrossRef](#)]
19. GB50010-2010; Chinese Code for Design of Concrete Structures. Ministry of Housing and Urban-Rural Development of the People's Republic of China (MOHURD): Beijing, China, 2015.
20. Mark, P.; Birtel, V. Parameterised finite element modelling of RC beam shear failure. In Proceedings of the 2006 ABAQUS Users Conference, Cambridge, MA, USA, 23–25 May 2006; pp. 95–108.
21. Zhu, J.-S.; Zhu, X.-C. Study on simplified method for the analysis of fatigue failure process of RC bridges. *Eng. Mech.* **2012**, *29*, 107–121. (In Chinese)
22. Guo, X.; Wang, Y.; Huang, P.; Chen, Z. Finite element modeling for fatigue life prediction of RC beam strengthened with prestressed CFRP based on failure modes. *Compos. Struct.* **2019**, *226*, 111289. [[CrossRef](#)]
23. Mohammad, A.; Houssam, T.; Tamer, E. Overload impact on the flexural behavior of RC strengthened with FRP composites under fatigue: Experimental study. *Eng. Struct.* **2020**, *211*, 111045.
24. Dineshkumar, R.; Ramkumar, S. Review paper on fatigue behavior of reinforced concrete beams. *Mater. Today Proc.* **2020**, *21*, 19–23. [[CrossRef](#)]
25. Niu, D.; Wang, Q. Models of concrete strength changing with time in general air environment. *Ind. Constr.* **1995**, *25*, 36–38. (In Chinese)
26. Yue, Q.; Wang, W.; Zhang, X. Study on time-dependent law of concrete compressive strength of existing buildings. *J. Shandong Jianzhu Univ.* **2023**, *38*, 9–14. (In Chinese)
27. Niu, D.; Wang, Q.; Wang, L. Estimation of steel corrosion in concrete in general atmospheric environment. *Eng. Mech.* **1997**, *14*, 92–99. (In Chinese)
28. Holmam, J.O. Fatigue of concrete by constant and variable amplitude loading. *ACI Spec. Publ. Fatigue Concr. Struct.* **1982**, *75*, 71–110.
29. Hsu, T.T.C. Fatigue of plain concrete. *ACI J.* **1981**, *2*, 292–305.
30. Zhang, B.; Phillips, D.V.; Wu, K. Further research on fatigue properties of plain concrete. *Mag. Concr. Res.* **1997**, *49*, 241–252. [[CrossRef](#)]
31. Alliche, A. Damage model for fatigue loading of concrete. *Int. J. Fatigue* **2004**, *26*, 915–921. [[CrossRef](#)]
32. JTG D60-2015; General Code for Design of Highway Bridges and Culverts. Ministry of Transport of the People's Republic of China: Beijing, China, 2015.

**Disclaimer/Publisher's Note:** The statements, opinions and data contained in all publications are solely those of the individual author(s) and contributor(s) and not of MDPI and/or the editor(s). MDPI and/or the editor(s) disclaim responsibility for any injury to people or property resulting from any ideas, methods, instructions or products referred to in the content.